



Isolated marginally stable geophysical vortices

Álvaro Viúdez†

Department of Physical Oceanography and Technology, Institute of Marine Sciences, CSIC, Barcelona 08003, Spain

(Received 6 February 2017; revised 19 June 2017; accepted 20 June 2017; first published online 17 July 2017)

Long-term marginal stability of a new family of isolated oceanic vortices is analysed. Sign reversal of the radial gradient of the potential vorticity anomaly, as implied by the isolation requirement, leads to vortex unsteadiness but does not break the coherence of the vortex, which remains marginally stable even for high absolute Rossby numbers $Ro \simeq 0.8$. The marginally stable vortices are characterized by a zero amount of potential vorticity anomaly on every isopycnal. The marginally stable final state is an unsteady vortex whose inner one-signed potential vorticity anomaly experiences revolution, rotation, precession and nutation.

Key words: geophysical and geological flows, vortex flows, vortex instability

1. Introduction

Baroclinic three-dimensional vortices are stable coherent structures in vertically stratified and horizontally rotating geophysical flows (e.g. Carton 2010). Persistence of these rotating structures has motivated the mathematical development of vortex models. Two convenient properties are often required in these vortex models, namely isolation from the background flow and stability to small perturbations. Vortex isolation implies that the amount of potential vorticity anomaly (henceforth PVA) in the vortex volume must sum up to zero, so that the radial PVA density distribution must change sign at some distance from the vortex centre in axisymmetric flows. The PVA density gradient must change sign as well. However, sign changing PVA density gradients lead to flow instability, and hence the paradox, noticed by Benilov (2003), arises, that geophysical vortex models, if isolated, must be unstable, a result apparently contradicting the long persistence of these vortices (e.g. Richardson, Bower & Zenk 2000). The purpose of this paper is to show that some isolated baroclinic vortices can develop flow instability and yet remain coherent for long time periods even for high Rossby numbers $Ro \equiv |\zeta|_{max}/f \simeq 0.8$, where ζ is the relative vertical vorticity and f is the planetary vorticity.

† Email address for correspondence: aviudez@cmima.csic.es

First, we introduce a new family of isolated vortices (§ 2) under the requirement of zero amount of PVA on every isopycnal. Mesoscale or submesoscale vortices are never found exactly isolated in the real ocean due to the ubiquitous existence of inertia–gravity waves, baroclinic tides, background horizontally and vertically sheared currents, surface wind stress, or even the close presence of other eddies or density fronts. Frequently, however, as suggested by the long persistence of these vortices, these external processes have only a perturbative second-order effect on the vortex dynamics, which justifies the investigation on theoretical models of baroclinic continuously stratified isolated vortices that remain stable to small perturbations. Furthermore, experimental data suggest that some long-life mesoscale subsurface eddies in the ocean display an outer PVA region of sign opposite to that of the vortex core (Paillet *et al.* 2002), which further supports the zero PVA amount vortex model.

The theoretical development and numerical algorithm used to analyse the vortex evolution and stability properties (§ 3) are based on a fully three-dimensional non-hydrostatic approach and on the explicit conservation of PVA on isopycnals. This PVA conservative method is therefore very well suited for this particular vortex application. The time evolution of a particular member of this vortex family (§ 4), with a high Rossby number $Ro \simeq 0.8$, and therefore out of the range of application of the quasigeostrophic (QG) approximation, and initially subjected to small perturbations, displays temporary growth of flow instabilities at the critical levels and subsequent inner-core vortex axisymmetrization. For high Rossby numbers, non-QG terms substantially affect the vortex stability properties (Tsang & Dritschel 2014). The final vortex state is, however, that of marginal stability, with an elliptic-like inner-core vortex experiencing precession and nutation, and forcing a second-mode vertical velocity field. Our purpose here is only to describe a representative case of an isolated marginally stable vortex with a high Rossby number, and no attempt is made to generate a stability classification, similar to that made in Yim, Billant & Ménesguen (2016), in the parametric space of this vortex family. Finally, concluding remarks are given in § 5.

2. Initial conditions: the vortex family $\overline{\omega}_{p,q}$

The vortex initial conditions define the stability properties of the vortex. We introduce the isolated vortex family $\overline{\omega}_{p,q}$ as a set of initial conditions having some members leading to marginally stable vortices. To avoid an excess of notation, the parameters (p, q) , whose meaning is explained below, are omitted, with a few exceptions, in the dependent variables symbols. Since the initial base conditions are axisymmetric and the vortices are defined in the isopycnal space, we work with isopycnal coordinates (τ, \mathfrak{z}) of radial distance τ and isopycnal \mathfrak{z} . The two-dimensional base PVA distribution $\tilde{\omega}_b(\tau, \mathfrak{z})$ satisfies the boundary conditions

$$\tilde{\omega}_b(0, \mathfrak{z}) = \tilde{\omega}_0(\mathfrak{z}), \quad \tilde{\omega}_b(\tau_0(\mathfrak{z}), \mathfrak{z}) = 0, \quad (2.1a,b)$$

where $\tilde{\omega}_0(\mathfrak{z})$ in (2.1a) defines the PVA profile along the vortex vertical axis and (2.1b) is required for PVA continuity at the vortex outer limit $\tau_0(\mathfrak{z})$. The radial dependence of $\tilde{\omega}_b$ is specified by its degree of smoothness along the radial direction at the vortex origin $\tau=0$ (parameter p) and at the vortex outer limit $\tau_0(\mathfrak{z})$ (parameter q) on isopycnals,

$$\frac{\partial^i \tilde{\omega}_b}{\partial \tau^i}(0, \mathfrak{z}) = 0, \quad i = 1, \dots, p, \quad \text{and} \quad \frac{\partial^j \tilde{\omega}_b}{\partial \tau^j}(\tau_0(\mathfrak{z}), \mathfrak{z}) = 0, \quad j = 1, \dots, q. \quad (2.2a,b)$$

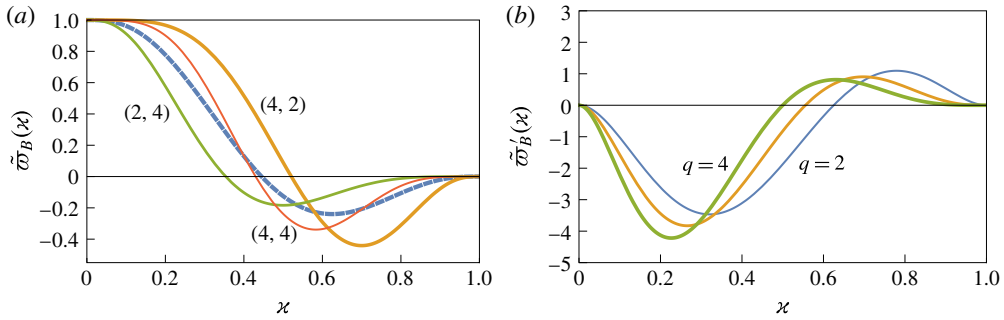


FIGURE 1. Four representative functions of (a) the base horizontal PVA $\tilde{\omega}_B(p, q; \kappa)$ and (b) its derivative $\tilde{\omega}'_B(p, q; \kappa)$ for $(p, q) = (2, 2)$ (dashed, not labelled), $(2, 4)$, $(4, 2)$ and $(4, 4)$.

Besides the above conditions we impose zero amount of PVA on every isopycnal layer,

$$\int_0^{\tau_0(\mathfrak{z})} \tilde{\omega}_b(\tau, \mathfrak{z}) \tau \, d\tau = 0. \tag{2.3}$$

Thus, the isopycnal gradient of the PVA assumes both signs along the vortex radius and satisfies the Charney–Stern necessary condition for the growth of disturbances (Charney & Stern 1962).

The PVA solution $\tilde{\omega}_b(\tau, \mathfrak{z})$ for monopolar one-core potential vorticity (PV) vortices with a single outer PV shield can be decomposed, in the isopycnal space, into horizontal and vertical components

$$\tilde{\omega}_b(\tau, \mathfrak{z}) = \tilde{\omega}_0(\mathfrak{z}) \tilde{\omega}_B(\tau/\tau_0(\mathfrak{z})). \tag{2.4}$$

In this equation, $\tilde{\omega}_B$ defines the horizontal spatial PVA distribution in terms of the radial distance τ normalized by the radius vortex $\tau_0(\mathfrak{z})$ on each isopycnal \mathfrak{z} , and is given (appendix A) by

$$\begin{aligned} \tilde{\omega}_B(\kappa) \equiv & 1 + \frac{(p+q+4)(p+1)}{2(q+1)} I(p+2, q+1; \kappa) \\ & - \frac{(p+q+2)(p+3)}{2(q+1)} I(p+1, q+1; \kappa), \end{aligned} \tag{2.5}$$

where $I(p, q; \kappa)$ is the normalized incomplete Beta function. Some examples of $\tilde{\omega}_B(p, q; \kappa)$ and its derivative $\tilde{\omega}'_B(p, q; \kappa)$ are shown in figure 1. It should be noted that we may generalize $p, q \in \mathbb{R}$ so that these symbols in (2.2) must be understood as their corresponding integer part. The function $\tilde{\omega}_0(\mathfrak{z})$ in (2.4) defines the PVA amplitude along the vortex vertical axis, or the vertical structure of the vortex. The simplest PVA surface geometry is spheroidal, so that both the normalized vortex horizontal radius $\tau_0(\mathfrak{z})/r_0$ and the normalized vertical axis PVA $\tilde{\omega}_0(\mathfrak{z})/\omega_0$ are given by the same function

$$\frac{\tau_0(\mathfrak{z})}{r_0} = \frac{\tilde{\omega}_0(\mathfrak{z})}{\omega_0} = \sqrt{1 - \frac{\mathfrak{z}^2}{\mathfrak{z}_0^2}}, \tag{2.6}$$

where constant $r_0 \equiv \tau_0(0)$ is the vortex radius at the middle isopycnal $\mathfrak{z} = 0$, $\omega_0 \equiv \tilde{\omega}_0(0)$ is the PVA at the vortex centre $(\tau, \mathfrak{z}) = (0, 0)$ and \mathfrak{z}_0 is the deepest vortex

isopycnal (located at a depth z_0 in the reference configuration, as explained in the next section). The vertical to horizontal vortex aspect ratio z_0/r_0 , the PVA at the vortex centre ϖ_0 and the horizontal structure parameters (p, q) complete the parameter set of the vortex family $\varpi_{p,q}$.

3. Numerical algorithm

The three-dimensional baroclinic geophysical (rotating and stably stratified) volume-preserving non-hydrostatic vortex flow, under the Boussinesq and f -plane approximations, is simulated using a triply periodic numerical model (Dritschel & Viúdez 2003) initialized using the PV initialization approach (Viúdez & Dritschel 2003). The PV is represented by contours lying on isopycnals. We use a 256^3 grid, with 256 isopycnals, in a domain of vertical extent $L_z = 2\pi$ (which defines the unit of length) and horizontal extents $L_x = L_y = cL_z$, where $c_0 \equiv 10$ is the ratio of the mean Brunt–Väisälä to the constant Coriolis frequency $c_0 \equiv N/f$. We take the buoyancy period (1 bp $\equiv 2\pi/N$) as the unit of time by setting $N \equiv 2\pi$. One inertial period (1 ip $\equiv 2\pi/f$) equals 10 bp. The time step $\delta t = 0.01$ and the initialization time $t_i = 5$ ip. The initialization time is the minimum time required for the fluid to reach its initial prescribed PVA state with minimal generation of inertia–gravity waves.

The vertical displacement \mathcal{D} of isopycnals with respect to the reference density configuration is $\mathcal{D}(\mathbf{x}, t) \equiv z - d(\mathbf{x}, t)$, where $d(\mathbf{x}, t) \equiv (\rho(\mathbf{x}, t) - \rho_0)/\varrho_z = \mathfrak{z}$ is the depth, or vertical location, that an isopycnal located at \mathbf{x} at time t has in the reference density configuration defined by $\rho_0 + \varrho_z z$, where ρ is the mass density and $\rho_0 > 0$ and $\varrho_z < 0$ are background density and background density stratification constants that do not need to be specified in this approach. It should be noted that \mathcal{D} is triply periodic but d is not. Static instability occurs when $\mathcal{D}_z \equiv \partial \mathcal{D} / \partial z > 1$. The Rossby number $\mathcal{R} \equiv \zeta / f$ and the Froude number $\mathcal{F} \equiv \omega_h / \mathcal{N}$, where ω_h and ζ are the horizontal and vertical components of the relative vorticity $\boldsymbol{\omega}$ respectively and \mathcal{N} is the total Brunt–Väisälä frequency. The PVA $\varpi \equiv \Pi - 1$, where $\Pi \equiv (\boldsymbol{\omega} / f + \mathbf{k}) \cdot \nabla d$ is the dimensionless total potential vorticity. The PVA ϖ is represented by contours in every isopycnal. The state variables are the components of the vector potential $\boldsymbol{\varphi} = (\varphi, \psi, \phi)$ that provide the velocity $\mathbf{u} \propto \nabla \times \boldsymbol{\varphi}$ and the vertical displacement of isopycnals $\mathcal{D} \propto \nabla \cdot \boldsymbol{\varphi}$. This approach, briefly described in appendix B and in detail in Dritschel & Viúdez (2003), has been applied to the study of a variety of ageostrophic flows in the atmosphere and oceans (e.g. Viúdez 2007).

4. Evolution of the isolated marginally stable vortex

In this section, we describe the time evolution of an oblate vortex $\varpi_{2,2}$, which is a smooth vortex compared with higher-order vortices having larger PVA gradients (figure 1). The main purpose of this section is to show that an initially perturbed $\varpi_{2,2}$ vortex experiences several unsteady processes, similar to those experienced by similar vortices, but it nevertheless remains marginally stable for long time periods. The specific $\varpi_{2,2}$ vortex chosen is a large-amplitude anticyclone with PVA amplitude $\varpi_0 = -0.8$, which implies a high maximum absolute Rossby number of $Ro \approx 0.8$ and oblate geometry $(r_0/c_0, z_0) = (2, -0.9)$ in the QG space of coordinates $(r/c_0, z)$. It should be noticed that, although the PVA distribution in the isopycnal space is oblate (figure 2a), the inner PVA core ($\tilde{\varpi}_B < 0$) is approximately spherical, and indeed the azimuthal velocity distribution $v_B(r, z)$ is prolate in the QG physical space (figure 2b). We notice that this particular parameter set $\{p, q, \varpi_0, |z_0 c_0 / r_0|\} = \{2, 2, -0.8, 0.9/2\}$ is an extremal case of a marginally stable vortex with a high Rossby number. Numerical

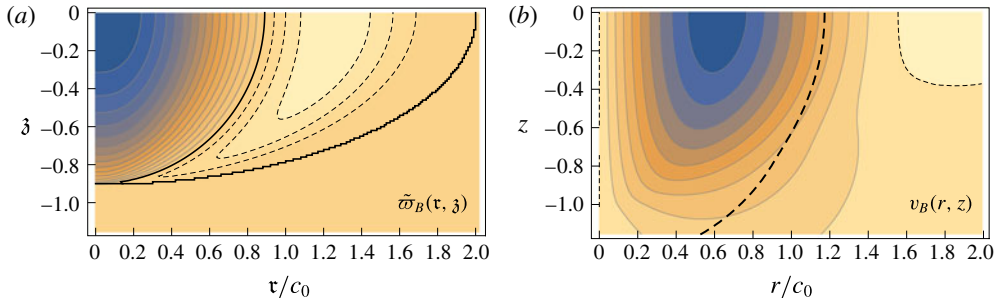


FIGURE 2. (a) The base 2D PVA $\tilde{\omega}_B(\tau, \mathfrak{z})$ for vortex $\varpi_{2,2}$. Contour lines $\tilde{\omega}_B < 0$ (continuous), $\tilde{\omega}_B = 0$ (thick) and $\tilde{\omega}_B > 0$ (dashed); contour interval $\Delta = 0.1$. (b) The base azimuthal velocity component $v_B(r, z)$. Contour lines $v_B < 0$ (continuous) and $v_B = 0$ (dashed); contour interval $\Delta = 0.1$; $v_B(r, z) \in [-0.97, 0.032]$. The thick dashed line indicates the critical level $r_{cr}(z)$ where $v_B(r_{cr}(z), z)/r_{cr}(z) = \dot{\vartheta}_0$. The spatial extent shown is only a part of the whole domain of the numerical simulation whose spatial intervals are $\Delta X/c_0 = \Delta Y/c_0 = \Delta Z = [-\pi, \pi]$.

experiments on vortices with larger z_0 (more prolate) or more negative ϖ_0 (higher Rossby number) turned out to be unstable, while vortices with shorter z_0 (more oblate) or less negative ϖ_0 (lower Rossby number) continued to be marginally stable. Increasing the parameters (p, q) with the other parameters remaining unchanged caused larger horizontal PVA gradients and resulted in unstable vortices. For example, both $\varpi_{3,3}$ and $\varpi_{4,4}$ vortices were unstable and, after breaking their positive and negative PVA cores, evolved, $\varpi_{4,4}$ more rapidly than $\varpi_{3,3}$, into two departing dipoles in a way similar to the two-dimensional zero circulation Rankine vortices in Morel & Carton (1994).

A small PVA jump $\delta\varpi \simeq 1.24 \times 10^{-2}$ is used to correctly discretize the PVA in the outer vortex. This small PVA jump implies a large number of PVA contours in every isopycnal. For example, the number of contours n_c between PVA extrema ϖ_0 and ϖ_{min} in the middle layer $\mathfrak{z} = 0$ (figure 3) is $n_c = 80$. The PVA minimum location (A 5) is $\chi_e = 5/8 = 0.625$ and its value $\varpi_{min} = \varpi(\chi_e, 0) \simeq -0.24$. Although numerical truncation inherent to any discrete computer algorithm causes a lack of precision and accuracy large enough to trigger the vortex unsteadiness at long times (e.g. Reinaud 2017), we added a small perturbation consisting of a small horizontal displacement of the PVA contours by an amplitude $\delta r = 0.1$ and vertical wavenumbers 2 and 3, in order to speed up the unsteady motion leading to the marginally stable vortex.

The time evolution of the vortex (figure 3, supplementary movie 1 available at <https://doi.org/10.1017/jfm.2017.440>) shows that, as expected, instability develops at the radius of maximum PVA, the critical level (Benilov 2003; Nguyen *et al.* 2012), and the inner core acquires a mode 2 perturbation. However, both the inner negative and outer positive PVA regions remain largely stable for long time periods. In this case, the vortex was stable through the complete simulation period of 365 ip, reaching Rossby numbers $\mathcal{R} \in [-0.77, 0.23]$ and maximum Froude number $\mathcal{F}_{max} = 0.24$.

Prior to the PVA wave breaking at the critical level, the inner vortex experiences layering (Nguyen *et al.* 2012; Hua *et al.* 2013; Meunier *et al.* 2015) above and below the middle depth (figure 4). Layering, or stacking of the PVA, as recently found by Nguyen *et al.* (2012), has a helical structure. Here, we observe, very clearly due to the large number of PVA contours on every isopycnal, the time evolution of the spiral

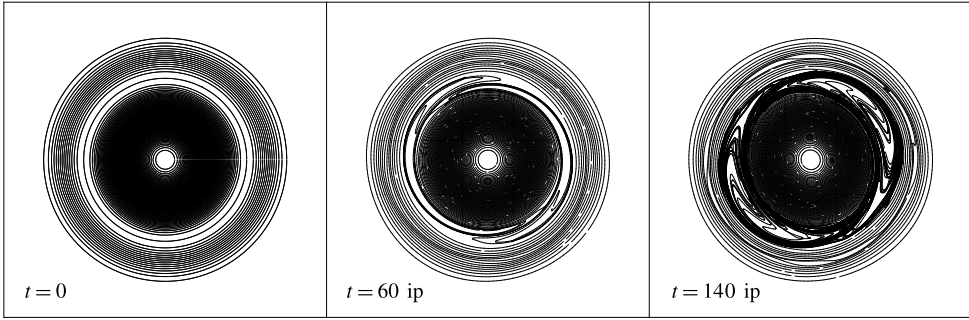


FIGURE 3. The distribution of the PVA jumps on the middle isopycnal $z = 0$ at times $t = 0, 60$ and 140 ip for vortex $\varpi_{2,2}$.

stacking consisting of a spiral with growing radial wavenumber. The spiral pattern is noticed as early as $t = 10$ ip with a radial wavenumber of approximately 2, and grows approximately as $t/(5 \text{ ip})$. It should be noted that layering occurs in most parts of the inner vortex and not only close to the critical level radius. These are probably vortex Rossby waves (Tung 1983; Montgomery & Kallenbach 1997; McWilliams, Graves & Montgomery 2003), taking place in the presence of PVA gradients and having an increasing radial wavenumber. The vortex Rossby waves develop and grow in the inner core but only break at the critical, or stagnation, radius, where the phase speed (given below) of the PVA mode 2 perturbation equals the angular velocity of the background azimuthal vortex motion. The averaged kinetic energy in the outer shell of positive PVA ($\varpi \geq 0.1$) increases at the expense of the potential energy of both this outer shell and the inner negative PVA vortex core.

Other vortex configurations, depending on the four parameters $\{p, q, \varpi_0, z_0 c_0/r_0\}$ of this vortex family, lead to vortices that become unstable and transform into a tripole, a pair of dipoles, etc., in ways similar to other vortices and dynamics described in previous studies (Carnevale & Kloosterziel 1994; Morel & Carton 1994; Reinaud 2017). These instability processes will not be analysed here.

In order to describe the unsteady PVA disturbances, we define the PVA centre of the inner vortex, at every depth z , by its normalized first moment $\hat{\mathbf{r}}_{\varpi}(z, t)$,

$$\hat{\mathbf{r}}_{\varpi}(z, t) \equiv \frac{\int_{S_h(z,t)} (xi + yj) \varpi(x, y, z, t) dx dy}{\int_{S_h(z,t)} \varpi(x, y, z, t) dx dy}, \quad (4.1)$$

where $S_h(z, t)$ is the spatial horizontal surface where $\varpi(x, y, z, t) < 0$ and its absolute value $|\varpi(x, y, z, t)|$ is larger than a threshold value $\varpi_T \equiv 0.1(|\max(\varpi)| + |\min(\varpi)|)/2$; that is, $S_h(z, t) = \{(x, y) \mid \varpi(x, y, z, t) \leq -\varpi_T\}$. The horizontal phase functions $\hat{\theta}(z, t) \equiv \arctan(\hat{\mathbf{r}}_{\varpi}(z, t) \cdot \mathbf{j}, \hat{\mathbf{r}}_{\varpi}(z, t) \cdot \mathbf{i})$ are not plotted since these are visually indistinguishable from a single straight line. The phase functions are vertically averaged to provide the averaged phase $\langle \hat{\theta} \rangle(t)$ and hence the averaged phase speed $\dot{\theta}(t) \equiv d\langle \hat{\theta} \rangle/dt$, which, using a linear model fit to $\langle \hat{\theta} \rangle(t)$, gives an average phase speed $\dot{\theta}_0 \simeq -0.3045 \text{ ip}^{-1}$, equivalent to a period $T_0 \simeq 20.63$ ip.

An alternative way to measure the phase speed of the PVA disturbance is through the vertical velocity field $w(x, y, z, t)$, which is an appropriate quantity to measure the

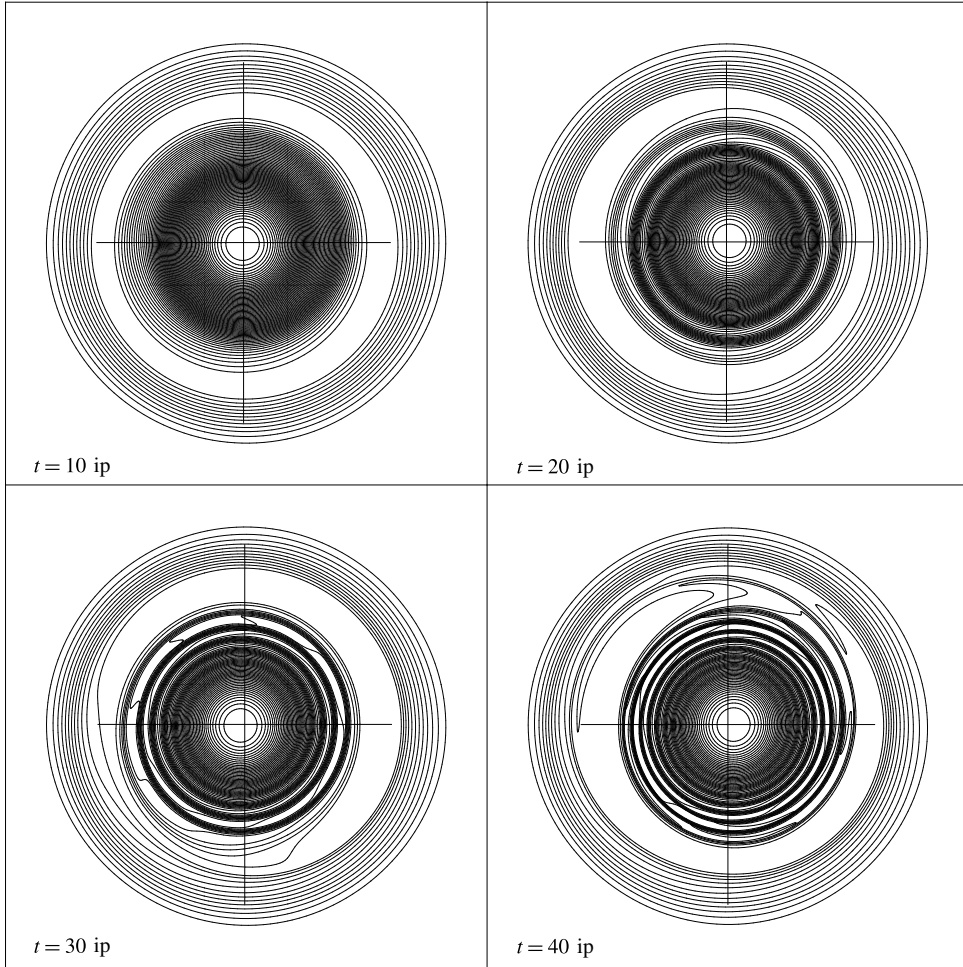


FIGURE 4. The distribution of the PVA jumps on the lower isopycnal $\bar{\sigma}_3 \simeq -0.4$ (isopycnal numerical index $i_3 = 102$) at times $t = 10, 20, 30$ and 40 ip for vortex $\varpi_{2,2}$. Vortex revolution is observed here as a slight mismatch between the vortex and domain geometrical centres.

vortex perturbation because the w of the vortex base state is zero, and w only develops due to the vortex deviation from its base state. The vertical velocity pattern (figure 5, movie 2) is basically dipolar and rotates with the vortex phase speed. Defining the positive and negative w centres $\mathbf{r}_{wh}^\pm(z, t)$, the mean location or vortex centre $\bar{\mathbf{r}}_{wh}(z, t)$ and the vector from negative to positive centres $\hat{\mathbf{r}}_{wh}(z, t)$ as

$$\mathbf{r}_{wh}^\pm(z, t) \equiv \frac{\int_{S_{\bar{r}}^\pm(z,t)} (x\mathbf{i} + y\mathbf{j})w(x, y, z, t) \, dx \, dy}{\int_{S_{\bar{r}}^\pm(z,t)} w(x, y, z, t) \, dx \, dy}, \quad (4.2)$$

$$\bar{\mathbf{r}}_{wh}(z, t) \equiv \frac{\mathbf{r}_{wh}^+(z, t) + \mathbf{r}_{wh}^-(z, t)}{2}, \quad \hat{\mathbf{r}}_{wh}(z, t) \equiv \mathbf{r}_{wh}^+(z, t) - \mathbf{r}_{wh}^-(z, t), \quad (4.3a, b)$$

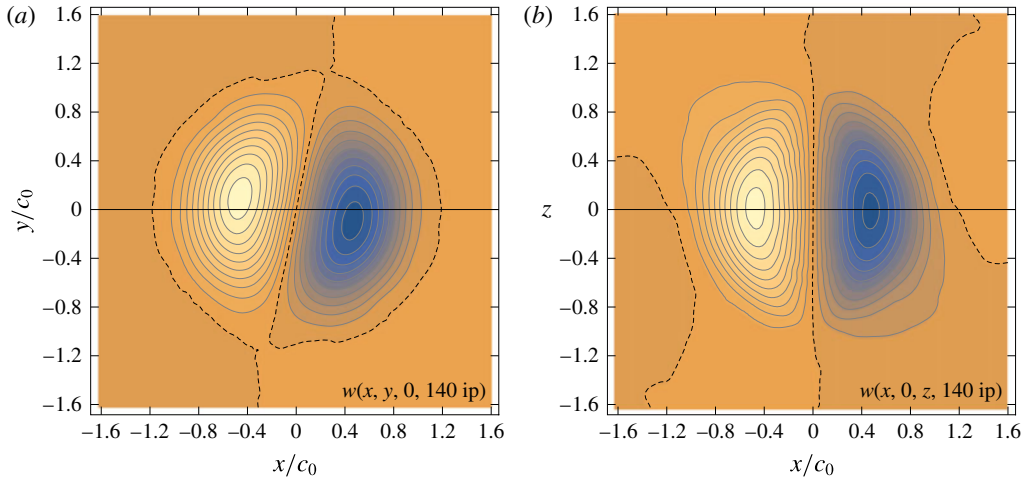


FIGURE 5. The vertical velocity $w(x, y, z, t)$ at time $t = 140$ ip on (a) the horizontal plane $z = 0$ and (b) the vertical section $y = 0$. Here, $w \in [-2.1, 2.1] \times 10^{-3}$ and the contour interval $\Delta = 0.2 \times 10^{-3}$.

it is also possible to trace the motion of the disturbance vortex. Above $S_h^\pm(z, t)$ is the spatial horizontal surface where the vertical velocity magnitude has a minimum threshold value $w_T \equiv 0.1(|\max(w)| + |\min(w)|)/2$; that is, $S_h^\pm(z, t) = (x, y) | \pm w(x, y, z, t) \geq w_T$. The phase velocity computed from the vertical velocity moments is very similar to $\hat{\theta}_0 \simeq -0.30 \text{ ip}^{-1}$. The critical radius r_{cr} is where the angular velocity $v(r_{cr}, z)/r_{cr} = \hat{\theta}_0$. At the plane $z = 0$, this happens at $r_{cr} \simeq 1.2c_0$, where $v(r_{cr}, 0) \simeq -0.3$. The critical radius $r_{cr}(z)$ decreases with depth z , and is included in figure 2(a).

The marginally stable vortex state is reached after an initial adjustment period of approximately 60 ip during which the vortex experiences the process of axisymmetrization towards a vertically tilted axial precession vortex. Vortex precession is a known process in unsteady baroclinic geophysical vortices (e.g. Päsche *et al.* 2012). The time evolution of the angle $\phi(z, t) \equiv \arctan(|\hat{r}_\omega(z, t)|/z)$ that forms the three-dimensional vortex axis vectors $\hat{r}_\omega(z, t) + z\mathbf{k}$ with the vertical direction \mathbf{k} (declination or axial tilt, figure 6a) shows the initial adjustment period, the axial precession with a mean declination $\langle\langle\phi\rangle\rangle \simeq 0.115$ (measured in the QG stretched space) and oscillations of $\langle\phi\rangle(t)$ around the mean $\langle\langle\phi\rangle\rangle$, which indicate nutation of the rotation axis. Visual inspection of $\langle\phi\rangle(t)$ in figure 6(a) reveals two kinds of nutations, namely a fast low-amplitude and a slow large-amplitude oscillation. The time spectrum of $\langle\phi\rangle(t)$ (figure 6b) confirms the two nutation frequencies $\vartheta_{n1} \simeq 0.023 \text{ cyc/ip}$ (period $T_{n1} \simeq 43.5 \text{ ip}$) and $\vartheta_{n2} \simeq 0.013 \text{ cyc/ip}$ (period $T_{n2} \simeq 76.9 \text{ ip}$), which are presumably related to the inner negative PVA vortex and outer positive PVA vortex respectively. It should be noted that both nutation periods T_{ni} are larger than the precession period $T_p \simeq 20.6 \text{ ip}$.

The inner vortex also experiences revolution, which may be noticed in figure 4 as a slight departure of the centre of the most interior vortex contour lines from the geometrical centre of the domain. Vortex revolution may be measured from the vertical average $\langle\hat{r}_\omega\rangle(t)$. The rotary spectra of $\langle\hat{r}_\omega\rangle(t)$ show that the revolution is anticyclonic with an amplitude of approximately 0.1 and period $T_R \simeq 20.9 \text{ ip}$, which, considering

Isolated marginally stable geophysical vortices

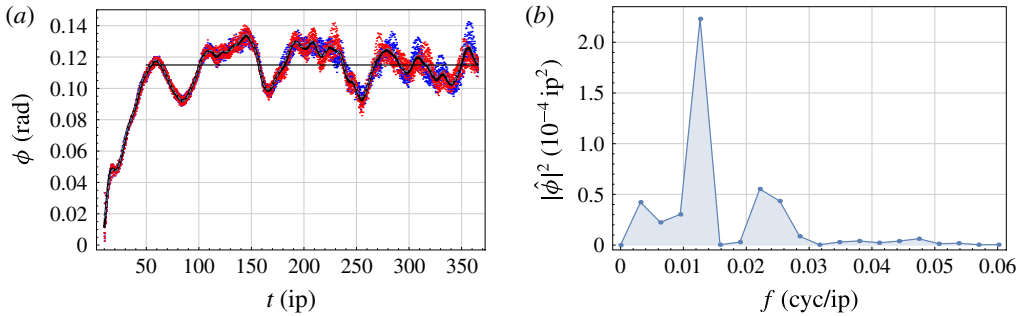


FIGURE 6. (a) The angle $\phi(z, t)$ computed from vectors in the lower ($z < 0$, blue points) and upper ($z > 0$, red points) part of the vortex. The black curve is the mean $\langle \phi \rangle(t)$, having a time-mean $\langle \langle \phi \rangle \rangle \simeq 0.115$. The grey dashed curve $\bar{\phi}(t) \simeq \langle \phi \rangle(t)$ is the angle of the straight line resulting from the least-squares fit to the locations $\hat{\mathbf{r}}_{\omega}(z_i, t) + z_i \mathbf{k}$ for z_i in the inner vortex. (b) The time spectrum of $\langle \phi \rangle(t)$, showing the two peaks at both nutation frequencies.

sampling errors (three-dimensional numerical fields are saved every inertial period), is indiscernible from the PVA vortex period $T_0 \simeq 20.6$ ip computed earlier, so that the vortex revolution and precession axis are in phase.

5. Concluding remarks

Long-term stability of isolated oceanic vortices has been a topic of fruitful research in fluid dynamics and physical oceanography in recent decades. Here, we have seen that, in some vortex configurations, sign reversal in the radial gradient of the PVA, as implied by the isolation requirement, leads to vortex unsteadiness but does not break the vortex coherence, and the vortex remains marginally stable even for high Rossby numbers. The marginally stable vortices are some elements of the new isolated vortex family $\varpi_{p,q}$ characterized by a zero amount of PVA on every isopycnal. Confidence in the numerical stability results is sustained by the reproduction of phenomena occurring in the vortex evolution towards the marginally stable final state. Spiral waves (apparently vortex Rossby waves) and axial symmetrization play an essential part in this evolution. The marginally stable final state is characterized by an unsteady vortex whose inner one-signed PV part experiences revolution, rotation, precession and nutation. Curiously, in this sense, the inner vortex experiences the same four motions as the solid Earth. Moreover, we do not discard flow instabilities that may break the vortex at very long times, say at $O(t) = 10^3$ ip, since we have not investigated this aspect with very long numerical integrations. However, at these very long time scales, the amplitude of ocean vortices decays due to turbulent viscosity or temperature and salinity diffusion, which are not considered in our PV conserving approach which is strictly valid for inviscid adiabatic flows.

In this marginally stable state, the vertical velocity has a dipolar pattern with maxima at $z = 0$. This dipolar pattern is related to the upward and downward motion of almost plane isopycnals caused by the axial precession of a spheroidal vortex. This dipolar pattern contrasts with the octopolar pattern of vertical velocity characteristic of ellipsoidal PVA, not precessing, vortices, which is due to the motion of fluid particles on ellipsoidal isopycnals at a speed faster than the vortex phase speed, and is therefore zero at $z = 0$ where isopycnals are horizontal.

The question of how well this mathematical vortex model fits oceanic vortices must be evaluated only after experimental acquisition and careful analysis of high-resolution density and velocity data, allowing detailed computation of the PVA along vortex vertical radial sections. We note that, although the vortex unsteadiness may look drastic in the PVA contours, the unsteady velocity perturbations are only of second order relative to the vortex flow. In the particular case analysed here, the maximum flow speed is of order $|\mathbf{u}| \approx 1$, while the corresponding speed perturbations are only $|\Delta \mathbf{u}| \approx 0.1$. Thus, experimental data analysis should be able to discriminate this intrinsic vortex velocity perturbation from external perturbations due to inertia–gravity waves, tides or wind stress induced currents.

Acknowledgements

I thank four anonymous referees for their very helpful comments. Partial support for this study was obtained through project CTM2014-56987-P (Spanish Ministry of Science and Innovation).

Supplementary movies

Supplementary movies are available at <https://doi.org/10.1017/jfm.2017.440>.

Appendix A. Base PVA distribution

The base PVA $\tilde{\omega}_b(\tau, \mathfrak{z})$ is constructed from the one-dimensional function $\varpi_B(\kappa)$, where the variable $\kappa = \tilde{\kappa}(\tau, \mathfrak{z}) \equiv \tau/\tau_0(\mathfrak{z})$ is the radial distance scaled by the vortex radius $\tau_0(\mathfrak{z})$ on isopycnal \mathfrak{z} . The function ϖ_B must satisfy boundary conditions

$$\varpi_B(0) = 1, \quad \varpi_B(1) = 0 \tag{A 1a,b}$$

and

$$\frac{d^i \varpi_B}{d\kappa^i}(0) = 0, \quad i = 1, \dots, p, \quad \frac{d^j \varpi_B}{d\kappa^j}(1) = 0, \quad j = 1, \dots, q, \tag{A 2a,b}$$

and the integral condition

$$\int_0^1 \varpi_B(\kappa) \kappa \, d\kappa = 0 \quad \Rightarrow \quad \int_0^1 \varpi_B'(\kappa) \kappa^2 \, d\kappa = 0. \tag{A 3a,b}$$

For monopolar vortices with a single PVA core and one PVA annulus of opposite PVA sign, the PVA ϖ_B on every isopycnal must have one zero and, subjected to the above conditions, only one interior extremum. Thus, $\varpi_B(\kappa)$ has only one interior extremum, say at $\kappa = \kappa_e$, and $\varpi_B'(\kappa)$ must be of the form

$$\varpi_B'(\kappa) \propto \kappa^p (1 - \kappa)^q (\kappa_e - \kappa). \tag{A 4}$$

The extremum κ_e is found from the integral condition (A 3b), resulting in

$$\kappa_e = \frac{\tau_e(\mathfrak{z})}{\tau_0(\mathfrak{z})} = \frac{B(p+4, q+1)}{B(p+3, q+1)} = \frac{p+3}{p+q+4}, \tag{A 5}$$

where $B(p, q)$ is the Beta function. Integration of (A 4), with boundary conditions (A 1a,b), leads to (2.5).

Appendix B. Theoretical basis of the numerical algorithm

By combining the non-hydrostatic balance of linear momentum in a rotating frame under the f -plane and Boussinesq approximations, the mass conservation equation and the isochoric condition we obtain the rate of change of $\mathcal{A} = \mathcal{A}_i + \mathcal{B}j + \mathcal{C}k \equiv \boldsymbol{\omega}/f - c_0^2 \nabla \mathcal{D}$,

$$\frac{d\mathcal{A}}{dt} = -f\mathbf{k} \times \mathcal{A}_h + (1 - c_0^2) \nabla w + \frac{\boldsymbol{\omega}}{f} \cdot \nabla \mathbf{u} + c_0^2 \nabla \mathbf{u} \cdot \nabla \mathcal{D}. \quad (\text{B } 1)$$

The horizontal component of (B 1), namely the rate of change of $\mathcal{A}_h = (\mathcal{A}, \mathcal{B})$, is numerically integrated using an explicit leapfrog scheme, together with a weak Robert–Asselin time filter to avoid decoupling between even and odd time levels. Spatial derivatives are carried out in the spectral space. A biharmonic hyperdiffusion term, providing a small damping rate (e folding) per ip at the highest wavenumber equal to $e_f = 50$, is added to the horizontal component of (B 1). The third prognostic equation is the explicit material conservation of PVA by contour advection on isopycnals ($d\varpi/dt = 0$), so that large PV gradients are not severely smoothed by diffusion. The locations of the PV contours are numerically integrated in time using a standard third-order three-time-level Adams–Bashforth scheme. The horizontal potentials $\boldsymbol{\varphi}_h = (\varphi, \psi)$ are recovered from the inversion, in the spectral space, of $\mathcal{A}_h = \nabla^2 \boldsymbol{\varphi}_h$, while the vertical potential ϕ is obtained from the inversion of the PVA definition $\varpi \equiv \Pi - 1 = (\boldsymbol{\omega}/f + \mathbf{k}) \cdot (\mathbf{k} - \nabla \mathcal{D}) - 1$ in terms of the potentials, $\varpi = \varpi_\varphi\{\varphi, \psi, \phi\}$. The main advantage of these prognostic equations is that they allow us to use the potential vector $\boldsymbol{\varphi}$, so that volume conservation is implicit, both three-dimensional velocity and vertical displacement are obtained directly from $\boldsymbol{\varphi}$, and the inversion of the horizontal potentials is easy (symbolically, $\boldsymbol{\varphi}_h = \nabla^{-2} \mathcal{A}_h$). The disadvantage of this formulation is that the computation of the (horizontal component) right-hand side of (B 1) and the inversion of the PVA (symbolically $\phi = \varpi_\varphi^{-1}\{\varphi, \psi, \varpi\}$) are numerically costly.

References

- BENILOV, E. S. 2003 Instability of quasi-geostrophic vortices in a two-layer ocean with a thin upper layer. *J. Fluid Mech.* **475**, 303–331.
- CARNEVALE, G. F. & KLOOSTERZIEL, R. C. 1994 Emergence and evolution of triangular vortices. *J. Fluid Mech.* **259**, 305–331.
- CARTON, X. 2010 Oceanic vortices. In *Fronts, Waves and Vortices in Geophysical Flows* (ed. J.-B. Flór), Lecture Notes in Physics, vol. 805, pp. 61–108. Springer.
- CHARNEY, J. G. & STERN, M. E. 1962 On the stability of internal baroclinic jets in a rotating atmosphere. *J. Atmos. Sci.* **19**, 159–172.
- DRITSCHEL, D. G. & VIÚDEZ, A. 2003 A balanced approach to modelling rotating stably-stratified geophysical flows. *J. Fluid Mech.* **488**, 123–150.
- HUA, B. L., MÉNESGUEN, C., GENTIL, S. L., SCHOPP, R., MARSSSET, B. & AIKI, H. 2013 Layering and turbulence surrounding an anticyclonic oceanic vortex: *in situ* observations and quasi-geostrophic numerical simulations. *J. Fluid Mech.* **731**, 418–442.
- MCWILLIAMS, J. C., GRAVES, L. P. & MONTGOMERY, M. T. 2003 A formal theory for vortex Rossby waves and vortex evolution. *Geophys. Astrophys. Fluid Dyn.* **97**, 275–309.
- MEUNIER, T., MÉNESGUEN, C., SCHOPP, R. & LE GENTIL, S. 2015 Tracer stirring around a meddy: the formation of layering. *J. Phys. Oceanogr.* **45**, 407–423.
- MONTGOMERY, M. T. & KALLENBACH, R. J. 1997 A theory for vortex Rossby-waves and its applications to spiral bands and intensity changes in hurricanes. *Q. J. R. Meteorol. Soc.* **123**, 435–446.

- MOREL, Y. G. & CARTON, X. J. 1994 Multipolar vortices in two-dimensional incompressible flows. *J. Fluid Mech.* **267**, 23–51.
- NGUYEN, H. Y., HUA, B. L., SCHOPP, R. & CARTON, X. 2012 Slow quasigeostrophic unstable modes of a lens vortex in a continuously stratified flow. *Geophys. Astrophys. Fluid Dyn.* **106** (3), 305–319.
- PAILLET, J., CANN, B. L., CARTON, X., MOREL, Y. & SERPETTE, A. 2002 Dynamics and evolution of a northern meddy. *J. Phys. Oceanogr.* **32**, 55–79.
- PÄSCHKE, E., MARSCHALIK, P., OWINOH, A. Z. & KLEIN, R. 2012 Motion and structure of atmospheric mesoscale baroclinic vortices: dry air and weak environmental shear. *J. Fluid Mech.* **701**, 137–170.
- REINAUD, J. N. 2017 Piecewise uniform potential vorticity pancake shielded vortices. *Geophys. Astrophys. Fluid Dyn.* **111** (1), 32–64.
- RICHARDSON, P. L., BOWER, A. S. & ZENK, W. 2000 A census of meddies tracked by floats. *Prog. Oceanogr.* **45**, 209–250.
- TSANG, Y.-K. & DRITSCHEL, D. G. 2014 Ellipsoidal vortices in rotating stratified fluids: beyond the quasi-geostrophic approximation. *J. Fluid Mech.* **762**, 196–231.
- TUNG, K. K. 1983 Initial-value problems for Rossby waves in a shear flow with critical level. *J. Fluid Mech.* **133**, 443–469.
- VIÚDEZ, A. 2007 The origin of the stationary frontal wave packet spontaneously generated in rotating stratified vortex dipoles. *J. Fluid Mech.* **593**, 359–383.
- VIÚDEZ, A. & DRITSCHEL, D. G. 2003 Vertical velocity in mesoscale geophysical flows. *J. Fluid Mech.* **483**, 199–223.
- YIM, E., BILLANT, P. & MÉNESGUEN, C. 2016 Stability of an isolated pancake vortex in continuously stratified-rotating fluids. *J. Fluid Mech.* **801**, 508–553.